

Generalizability of Graph Neural Network Force Fields for Predicting Solid-State Properties

Shaswat Mohanty^a, Yifan Wang^{a,b}, Wei Cai^{a,*}

^aDepartment of Mechanical Engineering, Stanford University, CA 94305-4040, USA

^bDepartment of Materials Science and Engineering, Stanford University, CA 94305-4040, USA

Abstract

Machine-learned force fields (MLFFs) promise to offer a computationally efficient alternative to *ab initio* simulations for complex molecular systems. However, ensuring their generalizability beyond training data is crucial for their wide application in studying solid materials. This work investigates the ability of a graph neural network (GNN)-based MLFF, trained on Lennard-Jones Argon, to describe solid-state phenomena not explicitly included during training. We assess the MLFF’s performance in predicting phonon density of states (PDOS) for a perfect face-centered cubic (FCC) crystal structure at both zero and finite temperatures. Additionally, we evaluate vacancy migration rates and energy barriers in an imperfect crystal using direct molecular dynamics (MD) simulations and the string method. Notably, vacancy configurations were absent from the training data. Our results demonstrate the MLFF’s capability to capture essential solid-state properties with good agreement to reference data, even for unseen configurations. We further discuss data engineering strategies to enhance the generalizability of MLFFs. The proposed set of benchmark tests and workflow for evaluating MLFF performance in describing perfect and imperfect crystals pave the way for reliable application of MLFFs in studying complex solid-state materials.

Keywords: Spectral Energy Density, Phonon Dispersion, String Method, Minimum Energy Path, Rare Events, Vacancy Diffusion

1. Introduction

Machine learning approaches to aid molecular dynamics (MD) simulations have developed rapidly in recent years. Techniques such as deep learning have been applied to accelerated MD simulations [1–4] to address their inherent time scale limitations. Creating accurate force fields has been a key area of development using deep learning architectures, often referred to as machine-learned force fields (MLFFs) or interatomic potentials (MLIPs). These models aim to achieve the scalability of classical MD simulations with the chemical accuracy of *ab initio* methods. Graph neural networks

*Corresponding author

(GNNs) are a common architecture choice for MLFFs to encode the local atomic environments. Starting from SchNet [5], developments along this direction subsequently lead to DeepMD [1, 6, 7]. The ability to differentiate between charged and uncharged species, needed for modeling ionic solvents, was introduced by ANI [8, 9] and further developed into SANI [10, 11] and QRNN [12] to capture complex behavior such as polarization and chemical reactivity [13]. These MLFFs and MLIPs have been used to study a number of systems such as metals [14–16], biomolecules [17], polymers [18] and organic molecules [19]. Our recent work presented a systematic approach for testing the transferability of these MLFF/MLIP models through the TB-MLFF library [20]. However, existing tests primarily focus on liquid-phase structures and dynamics. Our prior solid-phase tests were limited to the phonon density of states (PDOS) for a perfect crystal at zero temperature. Since a significant potential application of MLFF/MLIP models involves finite-temperature modeling of solid materials with defect-controlled properties, more rigorous testing in this domain is essential before trusting these models for predictive computational materials science applications.

This work introduces a more comprehensive set of solid-phase validation tests for MLFFs. We continue to use the GNN framework developed by Li et al. [21] to train an MLFF on data from the Lennard-Jones potential model of Ar, as a representative example. We extend our investigation beyond perfect crystals at zero temperature to include lattice vibration at finite temperatures and vacancy migration in imperfect crystals. On the finite-temperature lattice vibrations, we calculate the phonon dispersion relation, sensitive to both harmonic and anharmonic effects [22, 23], using the spectral energy density method (SED) [24–26] implemented in our C-XPCS library [27]. We also use the spectral energy density to estimate the thermal conductivity of the crystal [28] and benchmark the performance of the MLFF. On the defect dynamics in imperfect crystals, we calculate the vacancy jump rate from MD simulations using both the MLFF and the original potential model. The results are also compared against rate theory predictions [29] with activation energy barrier computed from a modified version of the string method [30–34]. These tests allow us to benchmark the MLFF in the solid phase and can help determine the modifications to the dataset that might be required to make the MLFF more generalizable.

The paper is organized as follows. Section 2 details the theoretical background of our methods. It describes the methods for computing the Hessian matrix and phonon density of states at zero temperature, as well as the methods for spectral energy density and thermal conductivity prediction at finite temperatures. It also describes the method for extracting vacancy jump rate from MD simulations, and the approach to estimate it from transition rate theories. Section 3 presents the results from our study, including the phonon dispersion curves and the vacancy diffusion rates obtained from both traditional and GNN-based MD simulations. Section 4 offers concluding remarks on our findings, and discusses potential future directions for using MLFF to investigate defects in solid materials.

2. Methods

2.1. Phonon density of states

The phonon density of states (PDOS) at zero temperature can be obtained from the eigenvalues of the Hessian matrix, \mathcal{H} , defined as,

$$\mathcal{H}_{ij} = \frac{\partial}{\partial x_j} \left(\frac{\partial U}{\partial x_i} \right) = -\frac{\partial f_i}{\partial x_j}, \quad (1)$$

where U is the potential energy, x_i is the coordinate of the i^{th} degree of freedom (i goes from 1 to $3N$ for a system of N atoms), and f_i is the atomic force acting on this degree of freedom. We note that MLFF does not provide the potential energy U , but directly predicts the forces f_i . The Hessian matrix can be obtained from numerical differentiation using a centered difference scheme,

$$\mathcal{H}_{ij} = \frac{f_i(x_j - \Delta x) - f_i(x_j + \Delta x)}{2\Delta x}, \quad (2)$$

In this work, we choose $\Delta x = 3.405 \times 10^{-4}$ Å (i.e. 10^{-4} in LJ unit) for the Hessian calculations using LAMMPS. While too large of a Δx can cause a substantial error in the numerical differentiation, care should be taken to ensure that Δx is not too small to cause numerical underflow, because MLFF usually uses single-precision floating point numbers.

The Hessian matrix \mathcal{H} as defined in Eq. (1) is expected to be symmetric ($\mathcal{H}_{ij} = \mathcal{H}_{ji}$) for a conservative force field that is derived from an interatomic potential U . This symmetry is exactly satisfied in the original Lennard-Jones potential. However, given that an MLFF does not provide the potential energy function U , this symmetry is not guaranteed and is worth checking. We define a measure for symmetricity, \mathcal{S} , as in [20], for a matrix A as

$$\mathcal{S}(A) = \frac{\|A_s\|_2 - \|A_a\|_2}{\|A_s\|_2 + \|A_a\|_2}, \quad (3)$$

where $\|\cdot\|_2$ indicates the Frobenius norm, and A_s and A_a are symmetrized and anti-symmetrized matrices defined as,

$$A_s = \frac{A + A^T}{2}, \quad (4)$$

$$A_a = \frac{A - A^T}{2}. \quad (5)$$

The symmetricity \mathcal{S} is bounded by $-1 \leq \mathcal{S}(A) \leq 1$, where $\mathcal{S}(A) = 1$ for a perfectly symmetric matrix and $\mathcal{S}(A) = -1$ for a perfectly anti-symmetric matrix. A good-quality MLFF should have its symmetricity $\mathcal{S}(\mathcal{H})$ as close to 1 as possible. We found that in our previous work, the choice of numerical differentiation step size Δx was too small (3.405×10^{-6} Å), which caused the computed Hessian matrix to be excessively asymmetric (see Table 3 of [20]).

Given the numerically computed Hessian matrix \mathcal{H} , we obtain the eigenvalues λ_n , $n = 1, \dots, 3N$, from its symmetrized matrix \mathcal{H}_s . Here N is the number of atoms in the simulation cell. The eigenfrequencies ν_n can be obtained from

$$\nu_n = \frac{1}{2\pi} \sqrt{\frac{\lambda_n}{m}}, \quad (6)$$

where m is the atomic mass (assuming all atoms have the same mass). The distribution of the ν_n corresponds to the PDOS. Furthermore, the Hessian matrix can also be used to obtain the phonon dispersion relation of the perfect crystal [35].

2.2. Spectral energy density

The PDOS and phonon dispersion calculations (based on the Hessian matrix) presented in the previous section rely on the harmonic approximation (HA) of interatomic interactions, which is strictly accurate only in the zero-temperature limit. Within HA, phonon modes have infinite lifetimes. However, at finite temperatures, phonon modes exhibit finite lifetimes. The spectral energy density (SED) method [24] allows for capturing the phonon dispersion relation at finite temperatures. The SED, $\phi(\mathbf{k}, \omega)$, measures the average kinetic energy per primitive cell as a function of wave vector \mathbf{k} , and the frequency ω , where $\omega = 2\pi\nu$. SED is computed by projecting the atomic trajectories in Molecular Dynamics (MD) simulation of a crystal on the normal vibrational modes of the lattice, as follows.

$$\phi(\mathbf{k}, \omega) = \frac{1}{4\pi\tau_0 N_T} \sum_a m \left| \int_0^{\tau_0} \sum_{n_{i,j,k}}^{N_T} \dot{u}_a(n_{i,j,k}; t) \cdot \exp[i\mathbf{k} \cdot \mathbf{r}_0(n_{i,j,k}) - i\omega t] dt \right|^2, \quad (7)$$

where τ_0 is the total simulation time, and N_T is the total number of primitive cells in the simulation cell. $N_T = N_x \times N_y \times N_z$, where N_x , N_y , and N_z refer to the number of primitive cells in the x , y , and z directions, respectively. $n_{i,j,k}$ denotes primitive cells with $i \in [1, N_x]$, $j \in [1, N_y]$, and $k \in [1, N_z]$. Eq. (7) is only applicable to crystals with a single-atom basis, such as the face-centered cubic (FCC) crystal of Ar considered here. \dot{u}_a stands for the atomic velocity in the a -th direction, where $a = x, y, \text{ or } z$. $\mathbf{r}_0(n_{i,j,k})$ denotes the equilibrium position of the $n_{i,j,k}$ -th primitive cell. The resulting $\phi(\mathbf{k}, \omega)$ map exhibits peaks at the (\mathbf{k}, ω) loci that correspond to the phonon dispersion relation.

To ensure accurate SED calculations using Eq.(7), the MD trajectory should cover a time period longer than the lifetime of the phonon mode of interest. For a phonon mode with wave vector \mathbf{k}_0 , the SED profile's peak (with respect to ω) can be fitted with a Lorentzian function to determine the phonon mode's lifetime,

$$\phi(\mathbf{k}_0, \omega) = \frac{\phi_{\max}}{1 + \left(\frac{\omega - \omega_c}{\gamma}\right)^2}, \quad (8)$$

where ϕ_{\max} is the peak value, ω_c is the peak frequency, and γ is the half-width at half maximum. From the fit, the phonon mode's lifetime can be estimated as $\tau = \frac{1}{2\gamma}$. The SED method serves as a valuable tool for assessing the accuracy of a force field in capturing lattice vibration statistics and reproducing the phonon dispersion relation and phonon lifetimes at finite temperatures.

Given the SED data, we can further predict the lattice thermal conductivity, κ , using the following expression [28].

$$\kappa = \sum_{(\mathbf{k}, \omega)} C_v(\omega) v_g^2(\mathbf{k}, \omega) \tau(\mathbf{k}, \omega). \quad (9)$$

where $C_v = \frac{k_B x^2 e^x}{V[e^x - 1]}$, $x = \frac{\hbar\omega}{k_B T}$ and V is the volume of the simulation cell. The sum is carried out over all $3N$ pairs of (\mathbf{k}, ω) that satisfy the phonon dispersion relation. \hbar is the reduced Planck's constant, k_B is the Boltzmann constant, and τ is the lifetime of the phonon in mode (\mathbf{k}, ω) . v_g is the group velocity which is obtained by evaluating the following derivative numerically along the phonon dispersion relation, $\omega(\mathbf{k})$.

$$v_g = \frac{d\omega}{dk} \quad (10)$$

where $k = \|\mathbf{k}\|$. Given the dependence of κ on the lifetime of the phonon in all the vibrational modes, the accurate estimation of κ serves as a rigorous test for an MLFF's ability to capture lattice dynamics.

2.3. Vacancy Jump Rates

We will use the tests described in the proceeding sections to measure the MLFF's ability to capture the lattice dynamics of a perfect crystal. To assess its performance for a defective crystal, we will focus on estimating the migration rate of a single vacancy.

To determine the vacancy migration rate, we conducted a long MD simulation (~ 53.9 ns) of a crystal containing a vacancy, tracking the vacancy's location over time. We then sample 100 short trajectories each with a starting time randomly chosen from the simulation. Defining $\chi(t)$ as the fraction of the vacancies that have not made a jump by time t in these sampled trajectories, we expect $\chi(t)$ to decay exponentially with time. By fitting $\chi(t) = \exp(-t/\tau_b)$, we obtain the vacancy jump rate, $r_j \approx 1/\tau_b$.

After identifying the vacancy jump rate at a given temperature T , we repeat the calculation at different temperatures. The resulting data are fitted to an Arrhenius expression,

$$r_j = \nu_0 \exp\left(-\frac{E_b}{k_B T}\right). \quad (11)$$

where ν_0 is the rate prefactor and E_b is the energy barrier. There are various ways to estimate the rate prefactor, such as the Eyring-Polanyi equation [29] and the harmonic transition state theory [36]. A rough estimate for the rate prefactor is the Debye frequency ν_D , which is related to temperature Θ_D by $\nu_D = k_B \Theta_D / h$, where $h = 2\pi\hbar$ is Planck's constant. Given that the Debye temperature for solid Argon is $\Theta_D = 92$ K [37],

the Debye frequency is $\nu_D = 1.92 \times 10^{12} \text{ s}^{-1}$. The energy barrier is the energy increase from the initial state (A) to the transition state (S), which can be separately predicted by minimum energy path (MEP) searches, such as the nudged-elastic band (NEB) method [38, 39]. These estimates of ν_0 and E_b serve as additional benchmarks to the MLFF’s ability to accurately capture vacancy jump rates.

3. Results

We present comparisons between the GNN-based MLFF and the original Lennard-Jones (LJ) potential on simulations of solid Argon, which forms a face-centered cubic (FCC) lattice at low temperatures. The GNN is trained on the LJ force field using samples containing both solid and liquid configurations (from 10 K to 105 K), similar to the previous models [27]. The solid configurations used in the training of GNN-based MLFF correspond to perfect crystals (i.e. vacancy-free) unless mentioned otherwise explicitly.

3.1. Phonon dispersion relations

As discussed earlier in Section 2.1, the Hessian matrix method can be used to obtain the phonon density of states at 0 K. Using a finite difference step size of $\Delta x = 3.4 \times 10^{-4} \text{ \AA}$ for the GNN-based MLFF, we obtain a nearly symmetric \mathcal{H} (the deviation of symmetricity \mathcal{S} from 1 is on the order of 10^{-5}). The coarser finite difference step size Δx doesn’t affect the agreement of the PDOS from the GNN-based MLFF against the reference LJ potential, as shown in Fig. 1. The mean absolute error (MAE) for each individual eigenfrequency (for the same eigenmode) is under 0.03 THz and the maximum absolute error (MaxAE) is less than 0.1 THz.

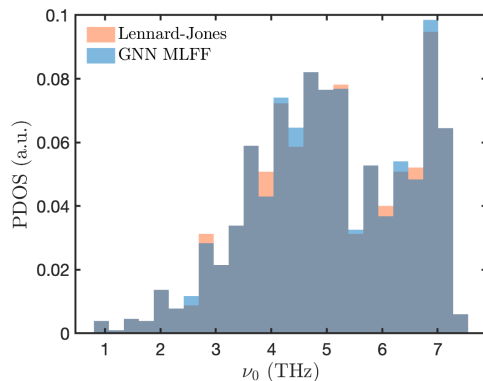


Figure 1: The phonon density of states at $T = 0 \text{ K}$ obtained from Lennard-Jones force field and the GNN-based force field with MAE of 0.02 THz and MaxAE of 0.09 THz.

We can obtain the \mathcal{H} and the subsequent PDOS at different pressures by imposing different pressures on the simulation cell. To test the accuracy and the generalizability of the \mathcal{H} obtained from the GNN-based MLFF, we compute the phonon dispersion

relation at 137.1 bar (the pressure of the simulation for the training configurations) and at -2.5 kbar, which represents unseen data for the model, as shown in Fig. 2. Under both pressures, the MAE and the MaxAE between each eigenfrequency (for the same eigenmode) are less than 0.1 THz.

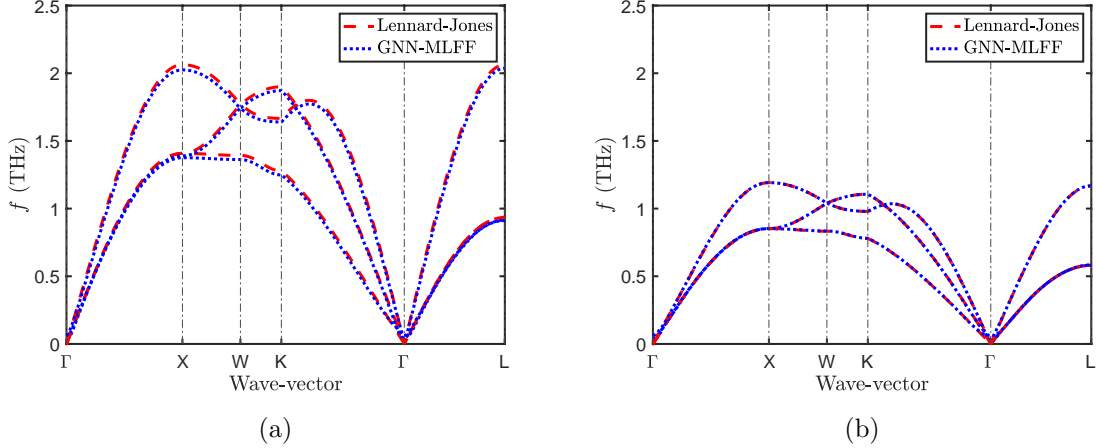


Figure 2: The phonon dispersion relation at $T = 0$ K obtained from the reference MD potential and the GNN-based MLFF at (a) $p = 137.1$ bar (training configuration pressure) with MAE of 0.02 THz and MaxAE of 0.07 THz and (b) $p = -2.5$ kbar with MAE of 0.002 THz and MaxAE of 0.06 THz.

The Hessian matrix allows us to calculate the phonon dispersion at 0 K where the phonons are trapped in a given mode of vibration (infinite lifetime). To obtain the phonon dispersion relation at a finite temperature where the phonons have a finite lifetime in any particular mode, we use the spectral energy density (SED) method (see Section 2.2). To this end, we consider a supercell that contains $5 \times 5 \times 100$ FCC unit cells, with a lattice parameter, $a = 4.808$ Å. The simulation cell is extended significantly in the z -direction to achieve a fine resolution in k_z . This quasi-1D configuration allows us to compute the phonon dispersion as a function of $k_z \in [-\pi/a, \pi/a]$ (from Γ point to X point in the reciprocal lattice). The initial configuration is relaxed to an energy minimum configuration by using the conjugate gradient algorithm, to obtain the equilibrium position, $\mathbf{r}(n_{x,y,z}, 0)$, for each primitive cell. We use the equilibrium position calculated by the LJ force field for the SED calculations for both the MD simulation and GNN-MD simulation trajectory. We first perform an NVT simulation thermostatted at 40 K (finite temperature) and adjust the simulation cell dimensions every 10 ps to reach the target pressure of $p = 137.1$ bar. We then obtain the equilibrium lattice constant of the crystal at finite temperature by performing energy relaxation. We finally perform an NVT simulation at the equilibrium box size for 100 ps, thermostatted at $T = 40$ K. The equilibrated configuration is used as the initial configuration for the MD and GNN-MD simulations, each carried out under an NVT ensemble thermostatted at 40 K for 107.8 ps, with configuration snapshots being recorded at 107.8 fs intervals. We use these 1000 frames to compute the phonon dispersion relation using the SED

analysis, which is sufficient since it is greater than the phonon lifetimes of solid Argon at this temperature.

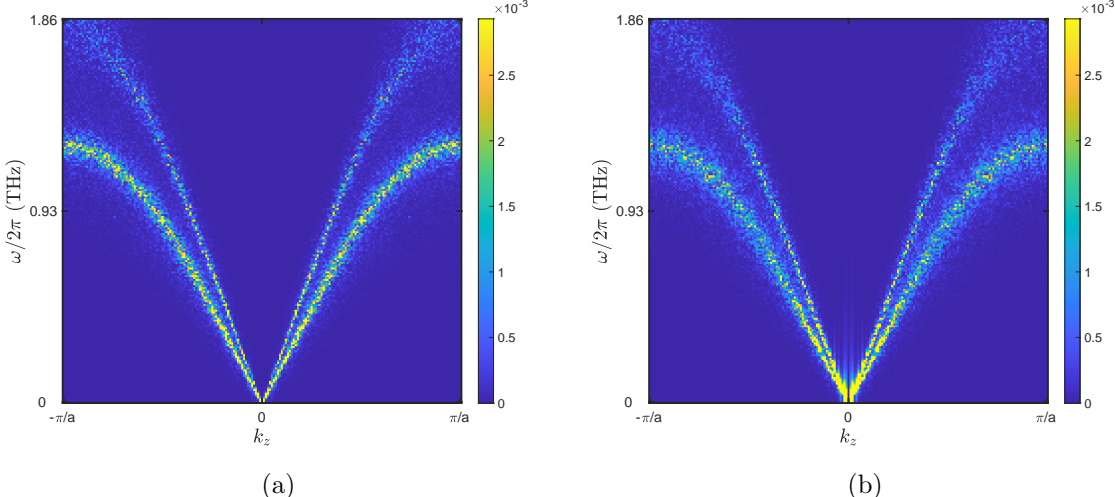


Figure 3: The spectral energy density, $\phi(\mathbf{k}, \omega)$, in eV·ps, at $T = 40$ K and $p = 137.1$ bar, obtained from the (a) MD simulation and (b) GNN-MD simulation trajectories.

The SED calculated from the MD and GNN-MD trajectory are in close agreement, as shown in Fig. 3, and the phonon dispersion relation obtained from the force constant matrix at 137.1 bar, indicating that the GNN-MD simulation is capable of capturing the acoustic and thermal properties of the system it is trained. The GNN-MD has some artificial oscillations in the SED only around small k_z values. In addition, we also compare the SED at $k_z = \pi/(10a)$ for frequencies under 1 THz and the averaged SED over a frequency range of 0.25 ± 0.02 THz for $k_z \in [-\pi/a, \pi/a)$, as shown in Fig. 4. The peaks in Fig. 4(a) correspond to the momentum of the phonon with an angular frequency of 0.25 THz. On the other hand, the inverse of the fitted peak widths in Fig. 4(b) corresponds to the phonon lifetimes, as described in and below Eq. (8). The phonon lifetime corresponding to the phonon mode with a momentum of $\hbar k_z$ obtained from the GNN-MD simulation is within 5% of the lifetime obtained from the MD simulation.

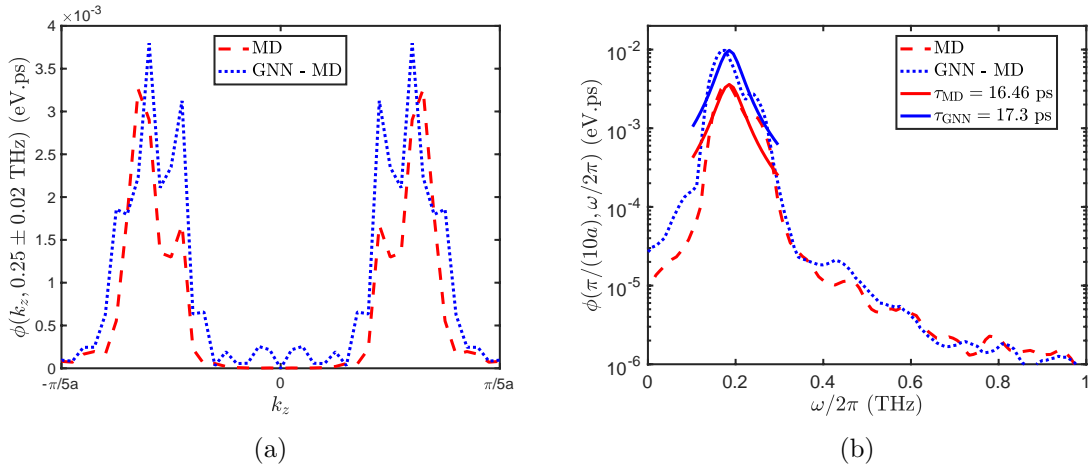


Figure 4: The spectral energy density, $\phi(\mathbf{k}, \omega)$, in eV·ps, at $T = 40$ K and $p = 137.1$ bar, (a) averaged over the frequency range of $\omega/2\pi = 0.25 \pm 0.02$ THz and (b) calculated at $k_z = \pi/(10a)$.

3.2. Thermal conductivity predictions

The SED signal generated from the MD and GNN-MD trajectory can be used to extract the thermal conductivity, κ , of the system using the relation in Eq. (9). We use a cubic simulation cell for the κ calculations, where the supercell is made of $10 \times 10 \times 10$ FCC unit cells and is thermostatted at 40 K and barostatted at a pressure of 137.1 bar. We limit the size of the simulation cell in the interest of the computational expense of the GNN-MD simulation. However, our results confirm that the simulation cell is large enough for a reliable estimate of κ . To validate the κ obtained from the SED calculations, we compare it against reference calculations from an MD simulation of a larger simulation cell, using the Green-Kubo formulation [40]. The reference simulation cell consists of $50 \times 50 \times 50$ FCC unit cells thermostatted at 40 K and barostatted at a pressure of 137.1 bar and the resulting thermal conductivity is $\kappa \sim 0.49$ W m⁻¹K⁻¹. From the SED calculations, we obtain $\kappa_{\text{MD}} \sim 0.45$ W m⁻¹K⁻¹ from the MD trajectory and $\kappa_{\text{GNN-MD}} \sim 0.55$ W m⁻¹K⁻¹ from the GNN-MD trajectory, which are both within 15% of the reference calculations. Overall, the phonon dispersion and thermal conductivity calculations from the MD and GNN-MD trajectories are in good agreement. These results provide an estimate of the quality of the GNN-based MLFF in thermal conductivity predictions and illustrate the value of these benchmarking tests for evaluating solid-state behavior in MLFF or MLIP models.

3.3. Vacancy jump rates

Having tested the performance of the MLFF for perfect crystals, we now present the analysis of the vacancy jumping rate in an imperfect crystal (containing a single vacancy). We started with a 256-atom solid configuration (in FCC lattice) and then removed one atom to create a vacancy. We also imposed a negative pressure of ~ 2.5 kbar, resulting in a low-density simulation cell at 5.711 mol/cm³. The low-density

simulation cell is chosen to reduce the energy barrier for vacancy jumps, so that they can be observed in the limited timescales accessible by MD and GNN-MD simulations. We use the resulting configuration to run MD and GNN-MD simulations for ~ 53.9 ns where we record the configuration snapshot every ~ 1.078 ps. We employ the Wigner-Seitz analysis using OVITO [41] to identify the vacancy in each configuration by comparing it to a perfect crystal configuration. A vacancy jump is recorded whenever the atom ID of the zero-occupancy atom changes in the Wigner-Seitz analysis.

We calculate the vacancy jump rate as described in Section 2.3. Fig. 5(a) shows the fraction χ of independent simulations in which the vacancy has not jumped as a function of time τ . The mean time for vacancy jumping, τ_b , is obtained by fitting $\chi(\tau)$ to $\exp(-\tau/\tau_b)$. We note that under this condition ($T = 60$ K) the mean jump time in GNN-MD is about a factor of 2 shorter than the original MD model, meaning that the vacancy jump rate predicted by the GNN-MD is about a factor of 2 greater than the original MD model. Nonetheless, that the GNN-MD predicts the vacancy jump rate within the same order of magnitude as that from the original MD model is an encouraging result, because it is common for rates to vary by orders of magnitude.

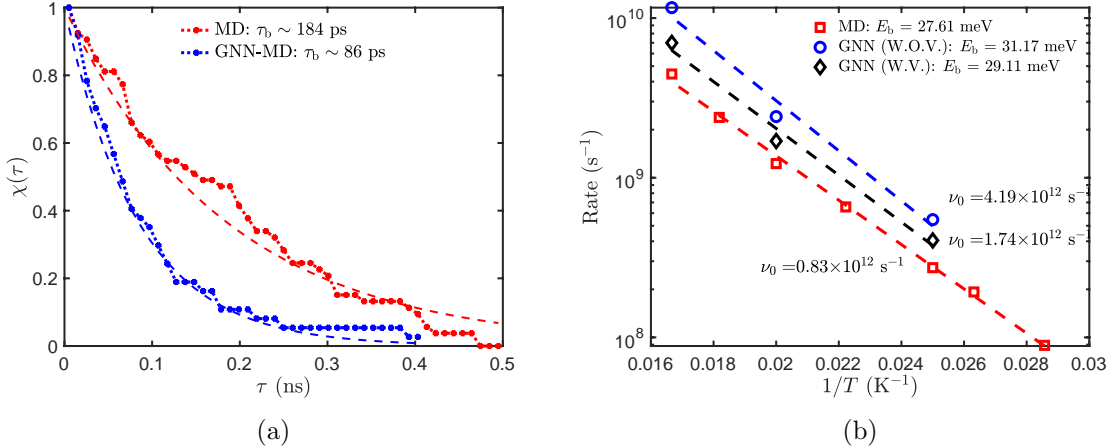


Figure 5: (a) The fraction of simulation trajectories in which the vacancy has not jumped as a function of time at $T = 60$ K from the GNN-MD (W.O.V.) simulation. (b) The Arrhenius plot of vacancy jumping rate as a function of $1/T$. GNN-MD (W.O.V.) and GNN-MD (W.V.) correspond to the MD simulation using the model trained on configurations without and with a single vacancy, respectively.

We repeat the calculation at different temperatures and extract the vacancy jump rate. Fig. 5(b) shows the Arrhenius plot of the rate as a function of inverse temperature predicted by the MD and GNN-MD simulation. Since the MD simulations are relatively inexpensive, they are carried out at 35 K, 38 K, 40 K, 45 K, 50 K, 55 K, and 60 K. On the other hand, the GNN-MD simulations are restricted to 40 K, 50 K, and 60 K. The predictions for each model can be well fitted by the Arrhenius expression, $r_j = \nu_0 \exp(-E_b/(k_B T))$, where ν_0 is the frequency prefactor and E_b is the energy barrier. The curve labelled as GNN-MD (W.O.V.) corresponds to the GNN-based

MLFF trained on solid and liquid configurations in which the solid is a perfect crystal that does not contain any vacancies. This is the same model used in all the previous plots, including Fig. 5(a). The curve labelled as GNN-MD (W.V.) corresponds to a GNN-based MLFF trained on solid and liquid configurations in which 15% of the dataset correspond to a crystal containing a single vacancy.

Our results show that both GNN-based models (with or without vacancy in the training data) are within 4 meV of the E_b predicted by the Arrhenius fit on the MD data of the original LJ potential. The frequency prefactor ν_0 computed from the GNN-MD simulations is within one order of the MD simulation results using the original LJ potential. The latter is also within one order of magnitude of the rough estimate provided by the Debye frequency ν_D . The GNN-MD simulations somewhat overpredict the vacancy jumping rate (hence ν_0) compared to the reference MD calculations. The inclusion of the vacancy configurations in the training data helps reducing the mismatch in the vacancy jump rates, as shown in Fig. 5(b). It is remarkable that the GNN-MD (W.O.V.) model, which did not see any vacancy configurations in a crystal during its training, performs reasonably well in terms of predicting the vacancy jump rates. Furthermore, it is unlikely that during training the GNN-MD (W.V.) model has seen any configurations corresponding to saddle configurations for vacancy jump (because of its rarity). Given that the activation energy of saddle configurations controls the vacancy jump rate (see Section 3.4), the improved agreement in the prediction of vacancy jump rate by the GNN-MD (W.V.) model with respect to the original MD model is also encouraging.

3.4. Energy barriers for vacancy jump

To benchmark the rates obtained from MD simulations against theories, we separately compute the energy barrier E_b by searching for the minimum energy path (MEP) for vacancy jump between two adjacent sites. First, we extract atomistic configurations from MD simulations at finite temperature, where the vacancy are located at two adjacent sites, as shown in Fig. 6(a). We then perform energy minimization (i.e. relaxation) starting from these configurations to obtain the local energy minima states, as shown in Fig. 6(b). The string relax method [34] is then used to obtain the MEP between these two configurations.

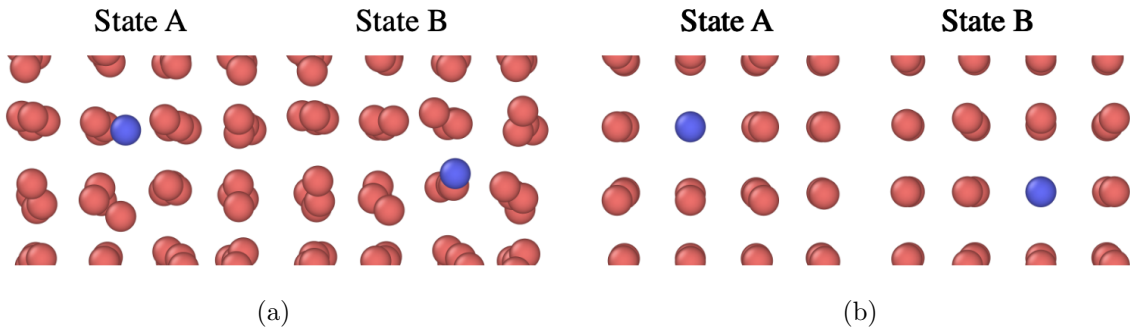


Figure 6: Initial and final configurations illustrating the vacancy jump (highlighted by the virtual blue atom). (a) Snapshots from MD simulations at $T = 40$ K. (b) Energy-minimized configurations used by the string relax method.

It is important to note that the GNN-MLFF predicts only the force for any atomic configuration but not the potential energy. Fortunately, the atomic forces are sufficient for the MEP search algorithm (e.g. the string method) to run. For example, when the algorithm converges, the atomic force should be parallel to the local tangent direction of the MEP everywhere along the path. After obtaining the MEP, we can numerically integrate the force along the path to obtain the energy barrier, as shown in Fig. 7.

The energy barrier obtained from MEP search is $E_b = 26.18$ meV for the original LJ potential, and $E_b = 25.95$ meV for the GNN-based MLFF (W.O.V.). Including the vacancy in the training data does not significantly affect the energy barrier, resulting in $E_b = 25.96$ meV for the GNN-based MLFF (W.V.). Again, it is worth noting that the GNN-based MLFF is able to capture the energy barrier of the vacancy jump even though the corresponding configuration has not been included in the training data.

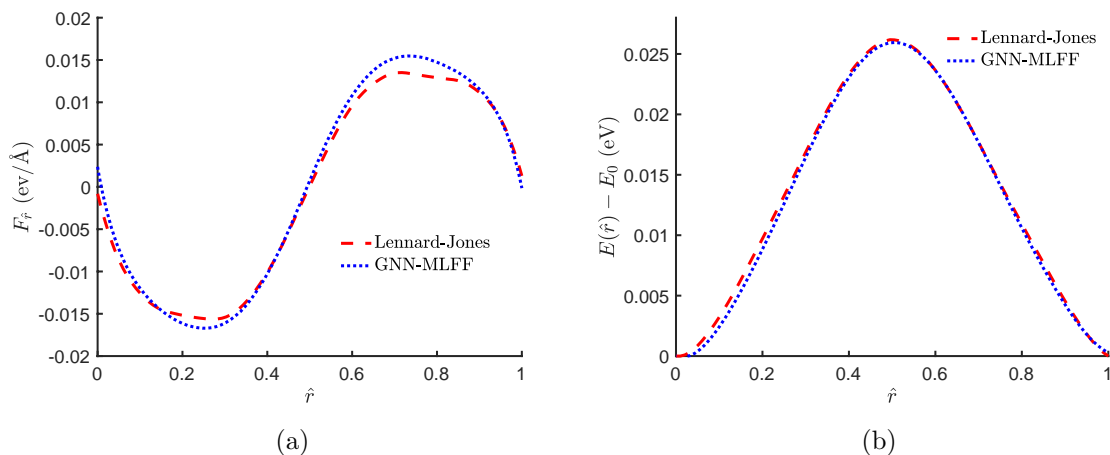


Figure 7: (a) Force along the MEP calculated by the LJ and GNN force calculators. (b) The energy barrier constructed by numerically integrating the force along the MEP, where $E_b = 26.18$ meV for the original LJ potential, and $E_b = 25.95$ meV for the GNN-based (W.O.V.) MLFF.

4. Conclusions

This paper presents an extensive set of tests that can be used to benchmark the transferability of machine-learned force fields or interatomic potentials for solid-phase simulations. We first demonstrate that the GNN-based MLFF is nearly conservative (i.e. the Hessian matrix is almost symmetric), and we use the Hessian matrix obtained from the MLFF to calculate the PDOS and phonon dispersion relation at 0 K. Furthermore, we compute the phonon dispersion relation using the spectral energy density (SED) method to capture the lattice vibrations at finite temperatures. The phonon dispersion relation and the thermal conductivity from the SED calculation obtained from the GNN-MD (using the MLFF) simulations agree well with the predictions from the original interatomic potential.

Our analysis is then extended to studying defects in the crystal, specifically, the jump rate of a single vacancy. We show that the vacancy jump rate GNN-MD simulations is of the same order of magnitude as the reference rate from the MD simulations. This suggests encouraging generalizability of the GNN-based MLFF model because it may be trained on configurations even without a vacancy. We employed the string relax method to calculate the minimum energy path for vacancy jumps. The resultant energy barrier from the original LJ and the GNN-based MLFF models is in close agreement, providing further evidence for the generalizability of the GNN-based MLFF model.

The tests presented here demonstrate the promise of MLFFs for studying defects in solids and rare events, which are important for applications in material science. These tests can be used to identify the modifications to the dataset that might be required to make the MLFF more generalizable, making high throughput and high-fidelity development of MLFF possible.

Conflict of Interest

The authors declare no competing interests.

Data Access

All data can be obtained on request from the corresponding author. The library for the testbed of machine-learned force fields can be found at [TB-MLFF](#).

Acknowledgements

S.M. and W.C. acknowledge support from the Precourt Pioneering Project of Stanford University. S.M. and W.C. acknowledge support from the Air Force Office of Scientific Research under award number FA9550-20-1-0397. We would like to thank Klara Suchan for the discussions on the spectral energy density method.

References

- [1] Han Wang, Linfeng Zhang, Jiequn Han, and E Weinan. Deepmd-kit: A deep learning package for many-body potential energy representation and molecular dynamics. *Computer Physics Communications*, 228:178–184, 2018.
- [2] Tianze Zheng, Weihao Gao, and Chong Wang. Learning large-time-step molecular dynamics with graph neural networks. *arXiv preprint arXiv:2111.15176*, 2021.
- [3] Hung N Do, Jinan Wang, Apurba Bhattarai, and Yinglong Miao. Glow: A workflow integrating gaussian-accelerated molecular dynamics and deep learning for free energy profiling. *Journal of Chemical Theory and Computation*, 18(3):1423–1436, 2022.
- [4] Danny Perez, Blas P Uberuaga, Yunsic Shim, Jacques G Amar, and Arthur F Voter. Accelerated molecular dynamics methods: introduction and recent developments. *Annual Reports in computational chemistry*, 5:79–98, 2009.
- [5] Kristof T Schütt, Huziel E Sauceda, P-J Kindermans, Alexandre Tkatchenko, and K-R Müller. Schnet—a deep learning architecture for molecules and materials. *The Journal of Chemical Physics*, 148(24):241722, 2018.
- [6] Aris Marcolongo, Tobias Binninger, Federico Zipoli, and Teodoro Laino. Simulating diffusion properties of solid-state electrolytes via a neural network potential: performance and training scheme. *ChemSystemsChem*, 2(3):e1900031, 2020.
- [7] IA Balyakin and AA Rempel. Machine learning interatomic potential for molten tizrhfnb. In *AIP Conference Proceedings*, volume 2313, page 030037. AIP Publishing LLC, 2020.
- [8] Justin S Smith, Olexandr Isayev, and Adrian E Roitberg. Ani-1: an extensible neural network potential with dft accuracy at force field computational cost. *Chemical science*, 8(4):3192–3203, 2017.
- [9] Justin S Smith, Roman Zubatyuk, Benjamin Nebgen, Nicholas Lubbers, Kipton Barros, Adrian E Roitberg, Olexandr Isayev, and Sergei Tretiak. The ani-1ccx and ani-1x data sets, coupled-cluster and density functional theory properties for molecules. *Scientific data*, 7(1):1–10, 2020.
- [10] James M Stevenson, Leif D Jacobson, Yutong Zhao, Chuanjie Wu, Jon Maple, Karl Leswing, Edward Harder, and Robert Abel. Schrodinger-ANI: An eight-element neural network interaction potential with greatly expanded coverage of druglike chemical space. *arXiv preprint arXiv:1912.05079*, 2019.
- [11] Leif D Jacobson, James M Stevenson, Farhad Ramezanghorbani, Delaram Ghorishi, Karl Leswing, Edward D Harder, and Robert Abel. Transferable neural

- network potential energy surfaces for closed-shell organic molecules: Extension to ions. *Journal of Chemical Theory and Computation*, 18(4):2354–2366, 2022.
- [12] Steven Dajnowicz, Garvit Agarwal, James M Stevenson, Leif D Jacobson, Farhad Ramezanghorbani, Karl Leswing, Richard A Friesner, Mathew D Halls, and Robert Abel. High-dimensional neural network potential for liquid electrolyte simulations. *The Journal of Physical Chemistry B*, 2022.
- [13] Connor W Coley, Wengong Jin, Luke Rogers, Timothy F Jamison, Tommi S Jaakkola, William H Green, Regina Barzilay, and Klavs F Jensen. A graph-convolutional neural network model for the prediction of chemical reactivity. *Chemical science*, 10(2):370–377, 2019.
- [14] Ivan Kruglov, Oleg Sergeev, Alexey Yanilkin, and Artem R Oganov. Energy-free machine learning force field for aluminum. *Scientific reports*, 7(1):8512, 2017.
- [15] Claudio Zeni, Kevin Rossi, Aldo Glielmo, and Francesca Baletto. On machine learning force fields for metallic nanoparticles. *Advances in Physics: X*, 4(1):1654919, 2019.
- [16] Volker L Deringer, Miguel A Caro, and Gábor Csányi. A general-purpose machine-learning force field for bulk and nanostructured phosphorus. *Nature communications*, 11(1):5461, 2020.
- [17] Paraskevi Gkeka, Gabriel Stoltz, Amir Barati Farimani, Zineb Belkacemi, Michele Ceriotti, John D Chodera, Aaron R Dinner, Andrew L Ferguson, Jean-Bernard Maillet, Hervé Minoux, et al. Machine learning force fields and coarse-grained variables in molecular dynamics: application to materials and biological systems. *Journal of chemical theory and computation*, 16(8):4757–4775, 2020.
- [18] Shaswat Mohanty, James Stevenson, Andrea R Browning, Leif Jacobson, Karl Leswing, Mathew D Halls, and Mohammad Atif Faiz Afzal. Development of scalable and generalizable machine learned force field for polymers. *Scientific Reports*, 13(1):17251, 2023.
- [19] David Rosenberger, Justin S Smith, and Angel E Garcia. Modeling of peptides with classical and novel machine learning force fields: A comparison. *The Journal of Physical Chemistry B*, 125(14):3598–3612, 2021.
- [20] Shaswat Mohanty, Sanghyuk Yoo, Keonwook Kang, and Wei Cai. Evaluating the transferability of machine-learned force fields for material property modeling. *arXiv preprint arXiv:2301.03729*, 2023.
- [21] Zijie Li, Kazem Meidani, Prakarsh Yadav, and Amir Barati Farimani. Graph neural networks accelerated molecular dynamics. *The Journal of Chemical Physics*, 156(14):144103, 2022.

- [22] Alberto Debernardi, Stefano Baroni, and Elisa Molinari. Anharmonic phonon lifetimes in semiconductors from density-functional perturbation theory. *Physical review letters*, 75(9):1819, 1995.
- [23] JE Turney, ES Landry, AJH McGaughey, and CH Amon. Predicting phonon properties and thermal conductivity from anharmonic lattice dynamics calculations and molecular dynamics simulations. *Physical Review B*, 79(6):064301, 2009.
- [24] John A Thomas, Joseph E Turney, Ryan M Iutzi, Cristina H Amon, and Alan JH McGaughey. Predicting phonon dispersion relations and lifetimes from the spectral energy density. *Physical Review B*, 81(8):081411, 2010.
- [25] Hao Ma, Erica O’Donnel, and Zhiting Tian. Tunable thermal conductivity of π -conjugated two-dimensional polymers. *Nanoscale*, 10(29):13924–13929, 2018.
- [26] JDC McConnell. Mt dove. introduction to lattice dynamics cambridge,(cambridge university press), 1993. xvii+ 258 pp., price£ 35. isbn 0 521 39293 4. *Mineralogical Magazine*, 59(396):581–582, 1995.
- [27] Shaswat Mohanty, Christopher B. Cooper, Hui Wang, Mengning Liang, and Wei Cai. Computational approaches to model x-ray photon correlation spectroscopy from molecular dynamics. *Modelling and Simulation in Materials Science and Engineering*, 8 2022.
- [28] Narges Naghdiani and Amir Abbas Sabouri Dodaran. Lattice thermal conductivity calculation of phosphorene using molecular dynamics and spectral energy density. *Solid State Communications*, 371:115263, 2023.
- [29] Henry Eyring. The activated complex in chemical reactions. *The Journal of Chemical Physics*, 3(2):107–115, 1935.
- [30] Keonwook Kang, Jie Yin, and Wei Cai. Stress dependence of cross slip energy barrier for face-centered cubic nickel. *Journal of the Mechanics and Physics of Solids*, 62:181–193, 2014.
- [31] William Kuykendall. *Investigating Strain Hardening by Simulations of Dislocation Dynamics*. PhD thesis, Stanford University, 2016.
- [32] Seunghwa Ryu, Keonwook Kang, and Wei Cai. Entropic effect on the rate of dislocation nucleation. *Proceedings of the National Academy of Sciences*, 108(13):5174–5178, 2011.
- [33] Seunghwa Ryu, Keonwook Kang, and Wei Cai. Predicting the dislocation nucleation rate as a function of temperature and stress. *Journal of Materials Research*, 26(18):2335–2354, 2011.

- [34] William P Kuykendall, Yifan Wang, and Wei Cai. Stress effects on the energy barrier and mechanisms of cross-slip in fcc nickel. *Journal of the Mechanics and Physics of Solids*, 144:104105, 2020.
- [35] G Kresse, J Furthmüller, and J Hafner. Ab initio force constant approach to phonon dispersion relations of diamond and graphite. *Europhysics Letters*, 32(9):729, 1995.
- [36] George H Vineyard. Frequency factors and isotope effects in solid state rate processes. *Journal of Physics and Chemistry of Solids*, 3(1-2):121–127, 1957.
- [37] GR Stewart. Measurement of low-temperature specific heat. *Review of Scientific Instruments*, 54(1):1–11, 1983.
- [38] Greg Mills and Hannes Jónsson. Quantum and thermal effects in h₂ dissociative adsorption: Evaluation of free energy barriers in multidimensional quantum systems. *Physical review letters*, 72(7):1124, 1994.
- [39] Gregory Mills, Hannes Jónsson, and Gregory K Schenter. Reversible work transition state theory: application to dissociative adsorption of hydrogen. *Surface Science*, 324(2-3):305–337, 1995.
- [40] Robert Zwanzig. Time-correlation functions and transport coefficients in statistical mechanics. *Annual Review of Physical Chemistry*, 16(1):67–102, 1965.
- [41] Alexander Stukowski. Visualization and analysis of atomistic simulation data with ovito—the open visualization tool. *Modelling and simulation in materials science and engineering*, 18(1):015012, 2009.